Supplementary Information

Iron-N-Heterocyclic Carbene Complexes as Efficient Electrocatalysts for Water Oxidation in Acidic Conditions

Wen-Xiu Guo,[a,d] Zhi-Kai Shen,[a] Yun-Fei Su,[a] Kang Li,[b] Wang-Qiang Lin,[c] Guang-Hui Chen,[c] Jie Guan,*[b] Xiaoming Wang,*[d] Zhaosheng Li,[a] Zhen-Tao Yu,*[a] and Zhigang Zou[a]

[a.] *National Laboratory of Solid State Microstructures and Jiangsu Provincial Key Laboratory for Nanotechnology, College of Engineering and Applied Sciences, Nanjing University, Nanjing, Jiangsu 210093, People's Republic of China. E-mail: yuzt@nju.edu.cn*

[b.] *School of Physics, Southeast University, Nanjing, Jiangsu 211189, People's Republic of China. E-mail: guanjie@seu.edu.cn*

[c.] *Department of Chemistry, Shantou University, Shantou, Guangdong 515063, People's Republic of China.*

[d.] *School of Life Sciences, Nanjing University, Nanjing, Jiangsu 210093, People's Republic of China. E-mail: wangxm07@nju.edu.cn*

Section 1: Materials and methods

Materials

2,6-Dibromopyridine, 1-methylimidazole, dry N,N-Dimethylformamide, ferrous chloride, potassium hexafluorophosphate, potassium tert-butoxide, sodium iodide, dichlorophenylborane, tetrabutylammonium bromide and trimethylsilyl trifluoromethanesulfonate were purchased from J&K Scientific Co., Inc. Dichloromethane, dry acetonitrile, acetone, methanol, hydrochloric acid, ether and nitric acid were purchased from Taicang hushi reagent Co., Ltd. Tetrabutylammonium hexafluorophosphate was obtained from Sigma-Aldrich Lab & Production Materials. $H_2{}^{18}O$ (97 atom% ^{18}O) was obtained from Aladdin Chemical Co., Ltd. All above solvents and reagents were used without further purification. Toluene (from Taicang hushi reagent Co., Ltd.) was distilled with add calcium hydride before used.

Synthesis

Tris(3-methylimidazolium-1-yl)(phenyl)borate bis(hexafluorophosphate) (L)

In glove box, dichlorophenylborane ($PhBCl_2$, 1.0 g, 6.3 mmol) was dissolve in 15 mL toluene. 1-methylimidazole (1.6 g, 19.7 mmol) was add to the above reaction flask under stirring. 20 mL toluene solution containing trifluoromethanesulfonate (3.2 g, 14.5 mmol) was added in the reaction flask after 15 min. The reaction flask was taken out of the glove box, and heated at 80 °C for 24 h with stir. After cooling to room temperature, a white solid was obtained and dissolved in dichloromethane. The solution was recrystallized under -32 °C. The ligand $PhB(MeImH)_3(OTf)_2$ by filtration.

The obtained ligand was treated into the corresponding hexafluorophosphate as following steps.[1] $PhB(MeImH)_3(OTf)_2$ (0.8 g, 1.2 mmol) was dissolved in acetone, mixed with 2 mL acetone solution with tetrabutylammonium bromide (0.8 g, 2.5 mmol). The relevant bromide salt was filtered and washed with acetone several times. The bromide ligand was dissolved in deionized water and mixed with 10 mL aqueous solution with ammonium hexafluorophosphate (2.5 mmol). The resulting white salt was filtered and washed with distilled water several times. **L** was obtained after drying under vacuum.

^{1}H NMR (500 MHz, CD_3CN) δ (ppm): 8.05 (s, 3H), 7.42 -7.48 (m, 6H), 7.15 (m, 2H), 7.11 (m, 3H), 3.81 (s, 9H).

2,6-bis(3-methylimidazolium-1-yl)pyridine (L')

2,6-dibromopyridine (6.4 g, 26.7 mmol) and 1-methylimidazole (8.6 mL, 106.9 mmol) were mixed in a reaction flask, and heated at 150 °C for 3h with reflux.[2] The solid was collected by filtration after cooling to room temperature. and washed with dichloromethane and diethyl ether for 3 times to remove impurities. The solid was dissolved in deionized water, and saturated ammonium hexafluorophosphate was added. **L'** was collected by filtration and dried under vacuum.

^{1}H NMR (500 MHz, CD_3CN) δ (ppm): 10.61 (s, 1H), 8.80 (s, 1H), 8.60(t, J = 8.1 Hz, 1H), 8.24 (d, J = 8.1 Hz, 1H), 8.0 (m, 1H), 4.04 (s, 2H).

2,6-bis(3-methylimidazolium-1-yl)pyridine-4-carboxylic acid (L'')

2,6-dibromopyridine-4 carboxylic acid (0.4 g, 1.3 mmol) and 1-methylimidazole (1.0 mL, 12.4 mmol) were added into a 100 mL reaction flask, and heated at 150 °C for 3h with reflux.[2] The product was collected by filtration after cooled to room temperature, and washed with 5 mL ether to obtain the crude product. The crude product was dissolved in methanol, and ether was added to precipitate white powder. The solid was dissolved in deionized water, and saturated ammonium hexafluorophosphate was added. **L''** was collected by filtration and dried under vacuum.

^{1}H NMR (500 MHz, CD_3CN) δ (ppm): 10.55 (s, 2H), 8.88 (s, 2H), 8.48 (s, 2H), 8.05 (s, 2H), 4.02 (s, 6H).

Synthesis of 1

Complex **1** was synthesized by the steps as reported by Sundström and coworkers with some modifications.[3] In glove box, L (200 mg, 0.3 mmol) and $FeCl_2$ (20 mg, 0.2 mmol) were dissolved in 3 mL of dry DMF solution. After stirring for 0.5 h, 200 mg (1.5 mmol) of potassium tert-butoxide was added in the solution and stirred for 10 min at room temperature. The reaction flask was taken out of the glove box, and stirred overnight in air. Red solution was obtained by filtration, and then saturated potassium hexafluorophosphate aqueous solution was added. Red solid was collected by filtration and washed with deionized water to remove excess hexafluorophosphate. The resulting residue was recrystallized from acetonitrile via slow diffusion of diethyl ether in the dark to yield rose-red crystals.

^{1}H NMR (500 MHz, CD_3CN) δ (ppm): 14.77 (s, 2H), 10.41 (t, J = 6.5 Hz, 2H), 9.76 (t, J = 7.4 Hz, 1H), 4.91 (s, 9H), 1.60 (s, 3H), 1.27 (s, 3H). ESI–HRMS (m/z): calculated for $C_{36}H_{40}B_2FeN_{12}$, 718.3034; found, 718.3039.

Synthesis of 2

L' (200 mg, 0.5 mmol) and $FeCl_2$ (30 mg, 0.2 mmol) were dissolved in 3 mL of dry DMF solution.[4] After stirring for 0.5 h, 200 mg (1.5 mmol) of potassium tert-butoxide was added in the solution and stirred for 10 min at room temperature. The pH was adjusted to 2 with dilute nitric acid and reacted overnight. Red solution was obtained by filtration, and then saturated potassium hexafluorophosphate aqueous solution was added. Red solid was collected by filtration and dissolved in acetonitrile. The diethyl ether was slowly diffused into the solution to precipitate single crystal (Fig. S1C).

^{1}H NMR (500 MHz, CD_3CN) δ (ppm): 8.18 (t, J = 8.1 Hz, 1H), 8.00 (s, 2H), 7.72 (d, J = 8.2 Hz, 2H), 6.99 (s, 2H), 2.51 (s, 6H). ESI–HRMS (m/z): calculated for $[C_{26}H_{26}FeN_{10}\text{-}(PF_6)]^+$, 679.1333; found, 679.1325.

Synthesis of 3

L'' (200 mg, 0.4 mmol) and $FeCl_2$ (25 mg, 0.2 mmol) were dissolved in 3 mL of dry DMF solution.[1] After stirring for 0.5 h, 200 mg (1.5 mmol) of potassium tert-butoxide was added in the solution and stirred for 10 min at room temperature. The pH was adjusted to 2 with dilute nitric acid and reacted overnight. Red solution was obtained by filtration, and then saturated potassium hexafluorophosphate aqueous solution was added. Red solid was collected

by filtration and washed with deionized water to remove excess hexafluorophosphate. The resulting residue was recrystallized from acetonitrile via slow diffusion of diethyl ether in the dark to precipitate single crystals.

^{1}H NMR (500 MHz, CD_3CN) δ (ppm): 8.30 (s, 1H), 8.15 (s, 1H), 7.01 (s, 1H), 2.49 (s, 6H). ESI–HRMS (m/z): calculated for $C_{28}H_{26}FeN_{10}O_4$, 311.0738; found, 311.0746.

Measurement apparatus

^{1}H NMR spectra were recorded on a Bruker AMX-500M NMR spectrometer. Atmospheric pressure chemical ionization mass spectrometry (APCI-MS) analysis was performed using a Thermo LCQ Fleet mass spectrometer. The EPR spectra were recorded on a Bruker EMX plus 10/12 (equipped with Oxford ESR910 Liquid Helium cryostat) spectrometer operating at X-band frequency (9.4 GHz) equipped with 100 kHz field modulation under 2K, and phase sensitive detection to obtain the first derivative signal. MS data were carried out on an Agilent 5973 Mass Selective Detector. The O_2 produced was determined by using an GC9720Plus Gas Chromatograph. Dynamic light scattering (DLS) was tested by a NanoBrook 90Plus Zeta (Brookhaven, USA). All data was measured 3 times through the system. Magnetic data were collected by MPMS XL-7. The elemental analysis experiment was completed on a Vario MICRO cube. The UV-vis absorption spectra measurements were performed in 3 mL quartz cells on a PerkinElmer LADBDA950 UV-Vis spectrophotometer. In situ spectroelectrochemistry was performed using a honeycomb quartz cell (*l* = 1 mm) with a Pine 200 electrochemical workstation, where gold honeycomb was used as the working and counter electrode, and a Ag/AgCl electrode (saturated KCl in deionized water, 0.197 V vs NHE) was used as reference electrode. Single crystal X-ray diffraction experiments were carried out at 193 K using a Bruker APEX-II CCD diffractometer. Using Olex2,[5] the structure was solved with the SHELXT[6] structure solution program using Intrinsic Phasing and refined with the SHELXL[7] refinement package using Least Squares minimization. The pH value of the liquid was determined by digital pH meter (PHS-3E, Shanghai Leici).

Electrochemical and catalytic water oxidation testing

The measurements were performed under ambient conditions in a three-electrode electrochemical system in a single-compartment cell in conjunction with a Pine 200 electrochemical workstation at room temperature. The cyclic voltammetry (CV) tests were carried out in acetonitrile solution with 0.1 M tetra-n-butylammonium perchlorate as the supporting electrolyte and 0.25 mM samples. The tests were performed using a standard three-electrode method with a glassy carbon electrode (GC electrode, rotating disc electrode with 5 mm diameter) as the working electrode (unless specifically indicated), Ag/AgCl as the reference electrode and a platinum (Pt) electrode as the counter electrode. CVs were recorded at a 50 mV s^{-1} scan rate, unless specifically indicated. A fresh glassy carbon electrode surface was prepared before each experiment by polishing with alumina powder and subsequently removing excess particles by sonication in ethanol and deionized water. In addition, electrodes were calibrated with potassium ferricyanide solution. Prior to measurements, the electrolyte solution was purged of air by bubbling with nitrogen for at least 20 min. Controlled potential electrolysis was also performed using a GC electrode (*d* = 3 mm) in a gas-tight cell (*V* = 25 mL) at a 50 mV s^{-1} scan rate. The kinetic isotope effects (KIE = k_{H2O}/k_{D2O}) were investigated in H_2O and D_2O, respectively. The hydrogen atom in phosphate is only 0.3 % of the total hydrogen atom in the system. ^{18}O-labeling experiments was carried out by using $H_2{}^{18}O$ for controlled potential electrolysis (0.25 mM complex **1** in a $H_2{}^{18}O$ (97 atom% ^{18}O)/acetonitrile (1:2) mixed solution with Et_4NClO_4 (0.1 M)

at 1.7 V vs NHE). The solution was deaerated by bubbling with N_2 gas for 30 min in gas-tight cell. The gas content in the headspace was determined by MS and GC. The onset potential in our manuscript was derived at the intersection point of the potential-axis and the tangent at the maximum slope of the current.[8] The overpotential was calculated from onset by the following eq. 2.

$$V_{NHE} = V_{Ag/AgCl} + 0.197\ \mathrm{V} \cdots\cdots\cdots\cdots\cdots\cdots\cdots (1)$$

$$\eta = V_{NHE} + 0.0591 \times \mathrm{pH} - 1.23\ \mathrm{V} \cdots\cdots\cdots\cdots\cdots (2)$$

Determine for turnover frequency (TOF).

The formula for the calculation of the turnover frequencies in the main text is derived from equations below.[9,10]

$$i_{cat} = n_{cat}\ \mathrm{FA[cat]}\sqrt{k_{cat}\mathrm{D}} \cdots\cdots\cdots\cdots\cdots\cdots\cdots (3)$$

$$i_p = 0.4463 n_p \mathrm{FA[cat]}\sqrt{\frac{n_p \mathrm{F} v \mathrm{D}}{\mathrm{RT}}} \cdots\cdots\cdots\cdots\cdots (4)$$

$$\frac{i_{cat}}{i_p} = \frac{n_{cat}}{0.4463 n_p}\sqrt{\frac{k_{cat} RT}{n_p F v}} \cdots\cdots\cdots\cdots\cdots\cdots\cdots (5)$$

In these equations, i_{cat} is the catalytic current, i_p is the peak current, n_{cat} is the number of electrons transferred in water oxidation (4 electrons), n_p is the number of electrons transferred associated with reversible electrochemical couples (1 electron), F is Faraday's constant, k_{cat} is the pseudo-first-order rate constant, R is the universal gas constant, T is the temperature in kelvin (at a room temperature of 298K), and v is the scan rate in V/s. The eq. 5 can be simplified to eq. 6 as listed in main text.

$$k_{cat} = 0.4847 v \left(\frac{i_{cat}}{i_p}\right)^2 \cdots\cdots\cdots\cdots\cdots\cdots\cdots (6)$$

The TOF (k_{cat}) can be calculated from Fig. 4 in main text by eq. 6.

Foot of the wave analysis (FOWA)

Equations obtained for i/i_p versus $1/\{1+\exp[(E_0\text{-}E)F/(RT)]\}$ (WAN, eq. 6) and versus $1/\{1+\exp[(E_0\text{-}E)F/(RT)]\}^{3/2}$ (I2M, eq. 7).[11] Corresponding plots are presented in Fig. S21.

$$\frac{i}{i_p} = \frac{4 \times 2.24 \left(\frac{RT}{Fv} k_{WNA}\right)^{\frac{1}{2}}}{1 + e^{\frac{F(E^0 - E)}{RT}}} \cdots\cdots\cdots\cdots\cdots\cdots\cdots (7)$$

$$\frac{i}{i_p} = \frac{4 \times 2.24 \left(\frac{RT}{3Fv} k_D C_{cat}^0\right)^{\frac{1}{2}}}{\left(1 + e^{\frac{F(E^0 - E)}{RT}}\right)^{\frac{3}{2}}} \cdots\cdots\cdots\cdots\cdots\cdots\cdots (8)$$

In these equations, F: Faradaic constant; R: gas constant; T: temperature; *i*: CV current intensity; i_p: peak current intensity of one-electron redox process of the catalyst; E_0: redox potential obtained by DPV; k_{WNA}: apparent WNA pseudo-rate constant; k_D: apparent dimerization constant.

Section 2: Characterization

As illustrated in Fig. S1a, complex **1** was efficiently synthesized from $FeCl_2$ and modified *tris*-NHC-carbene $(phtmeimb)^-$ with an incorporated phenyl group on the boron atom. During the Fe^{II} source react with tripodal mono-anionic *tris*-carbene ligands by a facial manner in air, Fe^{II} was automatically oxidized to Fe^{III}. Finally, the complexes are treated with ammonium hexafluorophosphate to produce the corresponding hexafluorophosphate.

The X-ray crystal structure (Fig. S1b) reveals that Fe^{III} is in the center of **1**, which is held by six coordinating NHC moieties from two [phenyl(*tris*(3-methylimidazol-1-ylidene))borate]$^-$ ligands to form octahedral coordination. Mass spectrometry (Fig. S2) affords a prominent peak at m/z 718.3039, corresponding to $[Fe(phtmeimb)_2]^+$ (theoretical value is 718.3034). These results are consistent with the report by Sundström and coworkers.[3] The X-ray crystal structure of complex **2** (Fig. S1c) shows same result as reported by Wärnmark and coworkers.[12] All the final complexes were characterized by ^1H NMR spectroscopy as shown in Fig. S3-S5.

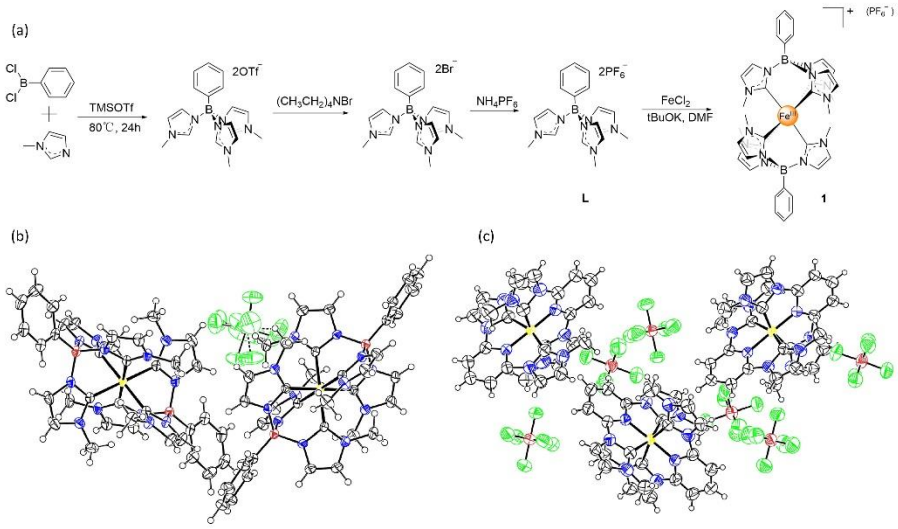

Fig. S1 (a) Synthesis process of complex **1**. (b) X-ray crystal structure showing thermal ellipsoid plot of complex **1**. (c) X-ray crystal structure showing thermal ellipsoid plot of complex **2**. Color scheme: Fe (yellow), B (red), N (blue), F (green), C (black), H (black hollow).

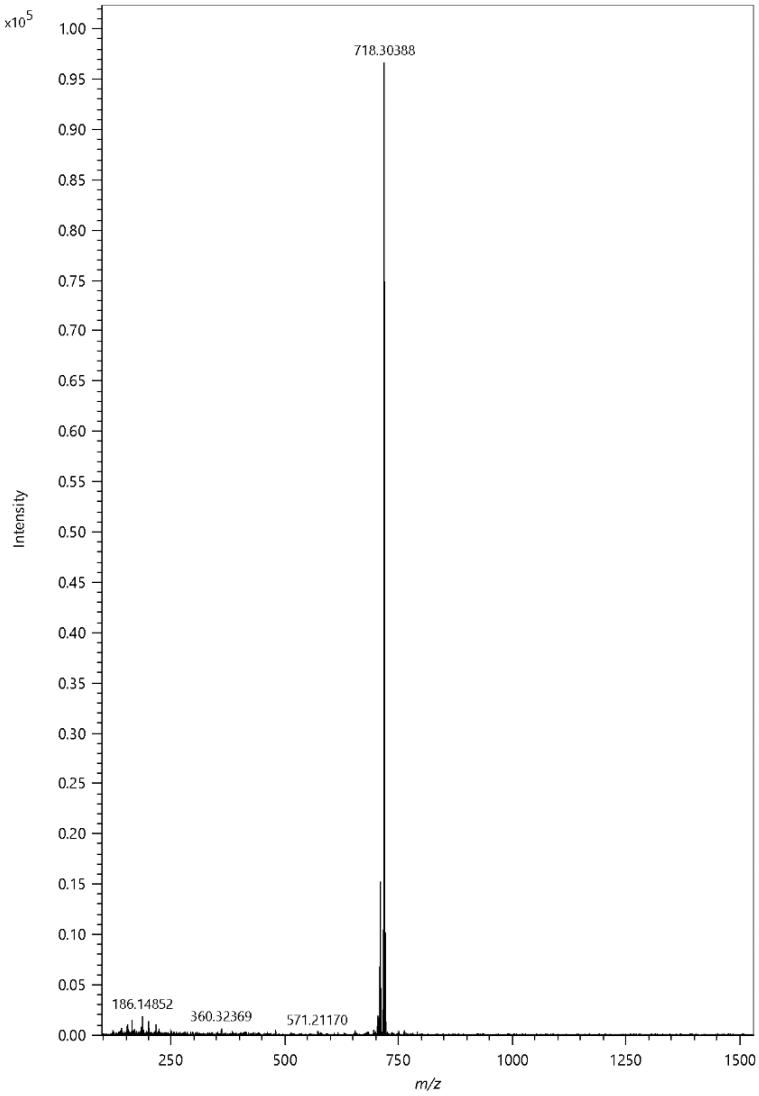

Fig. S2 HR-MS spectrum of complex **1**.

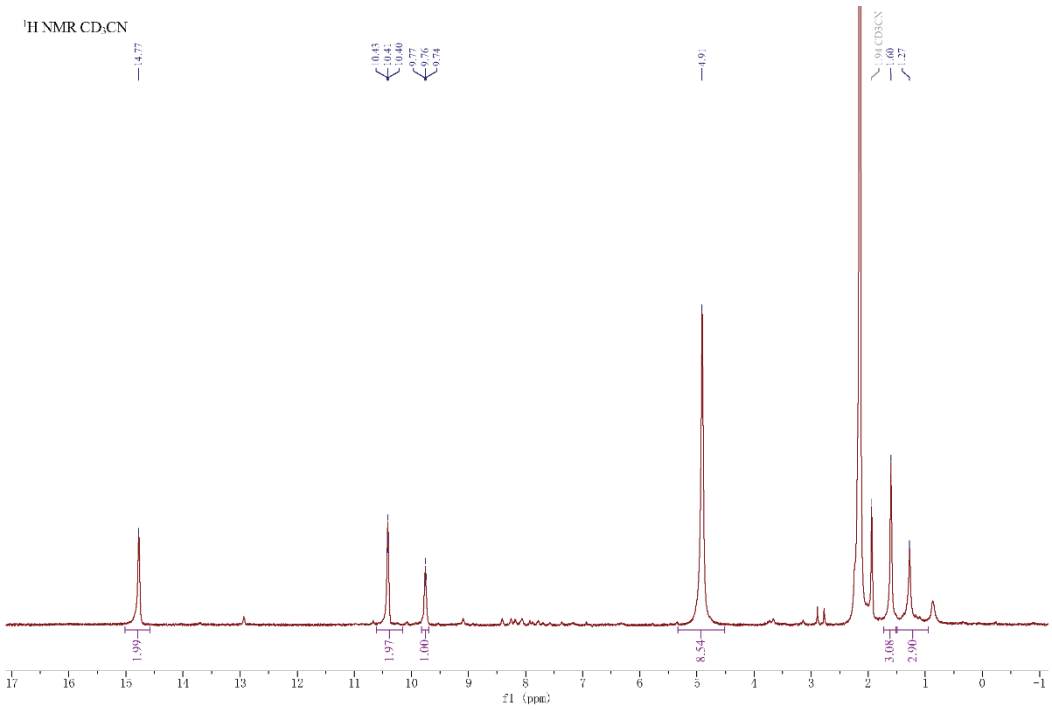

Fig. S3 ^{1}H NMR of **1** in CD_3CN. Resonances at 1.94 represent trace amounts of CD_3CN.

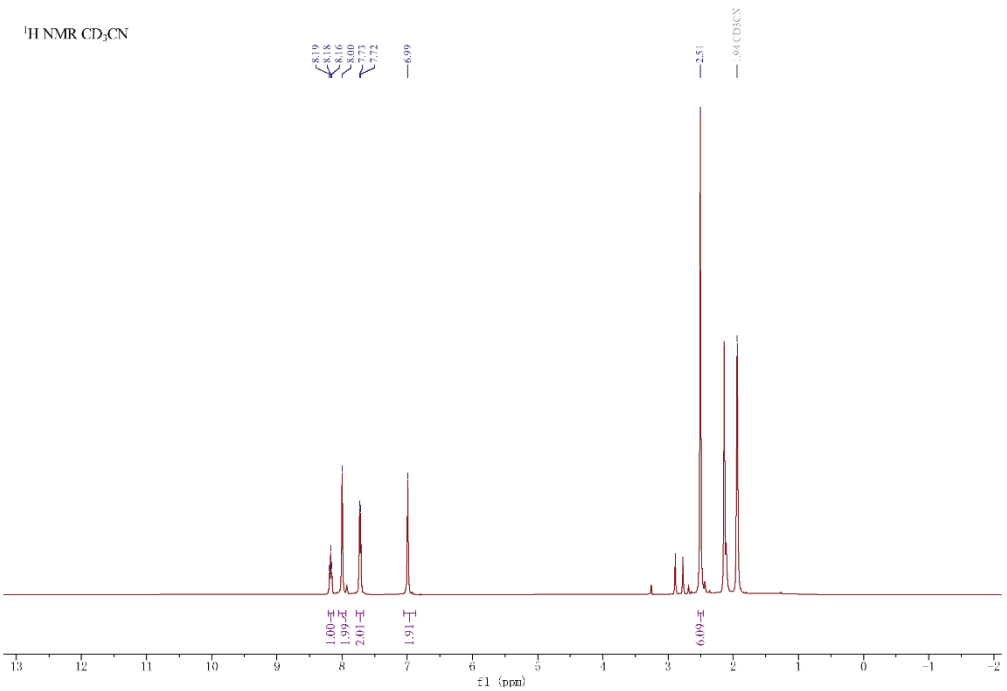

Fig. S4 ^{1}H NMR of **2** in CD_3CN. Resonances at 1.94 represent trace amounts of CD_3CN.

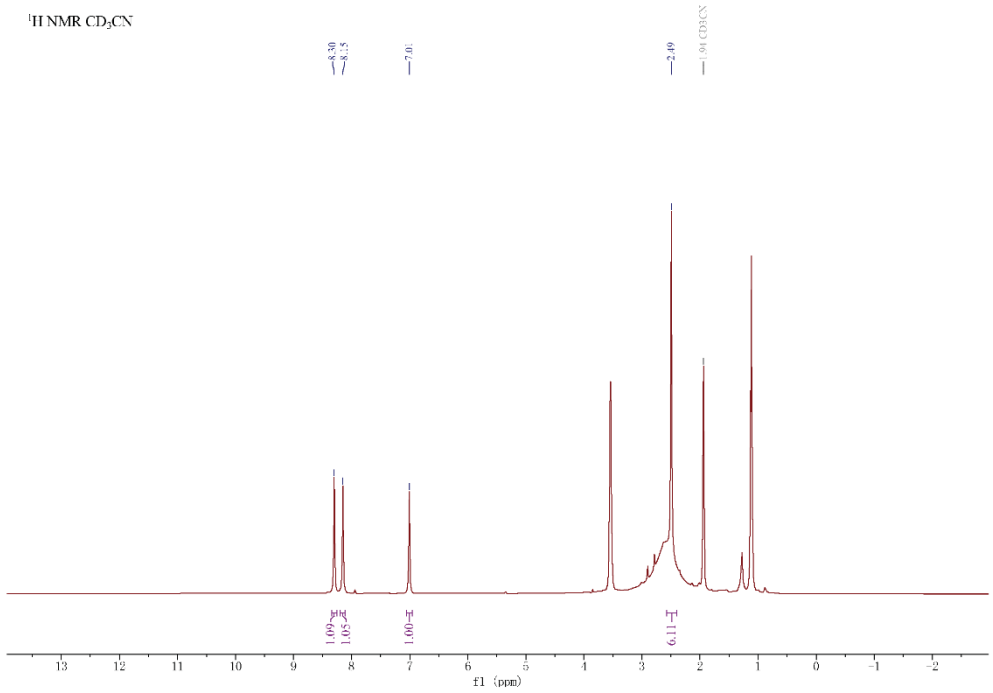

Fig. S5 ^{1}H NMR of **3** in CD_3CN. Resonances at 1.94 represent trace amounts of CD_3CN.

Table S1. Summary of the crystallographic and structure data for **1** (PF_6).

Empirical formula	$C_{36}H_{40}B_2F_6FeN_{12}P$
Formula weight	863.24
Temperature, K	193.0
Wavelength, Å	1.34139
Crystal system	triclinic
Space group	P-1
A (Å)	9.9581 (4)
B (Å)	11.3847 (4)
C (Å)	19.6671 (7)
α (deg)	88.8930 (10)
β (deg)	85.958 (2)
γ (deg)	89.816 (2)
Volume $Å^3$	2223.69 (14)
Z	2
Density (g / cm^3)	1.289
Absorption coefficient (mm^{-1})	2.462
F (000)	890.0
Theta range for data collection	3.92 to 121.104°
Index ranges	-12 ≤ h ≤ 12, -14 ≤ k ≤ 14 -25 ≤ l ≤ 24
Reflections collected	29328
Independent reflections	9968 [R(int) = 0.0511]
Goodness-of-fit on F2	1.043
Goodness-of-fit on F2	1.043
Data / restraints / parameters	9968/136/579
Final R indices [I > 2 σ (I)]	R_1 = 0.0452, wR_2 = 0.1302
R indices (all data)	R_1 = 0.0511, wR_2 = 0.1341

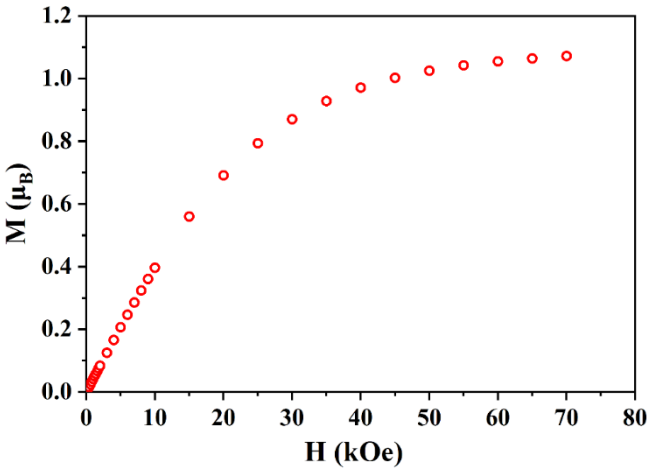

Fig. S6 Field-dependent isothermal magnetization for complex **1** at T = 2 K.

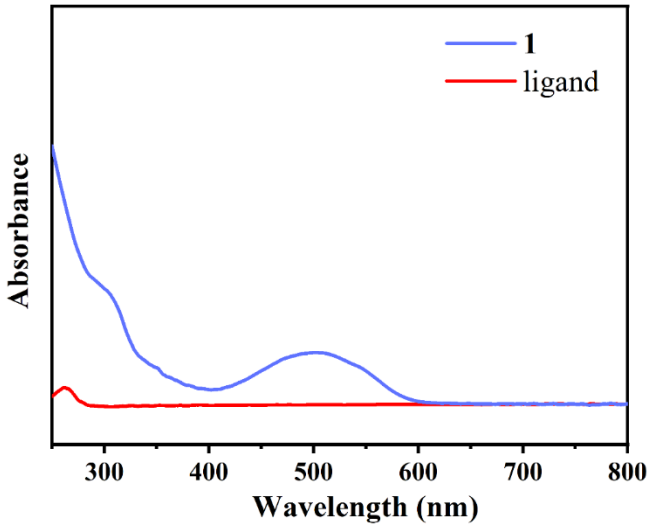

Fig. S7 UV-vis absorption of **1** and **L** (ca. 0.1mM) in acetonitrile.

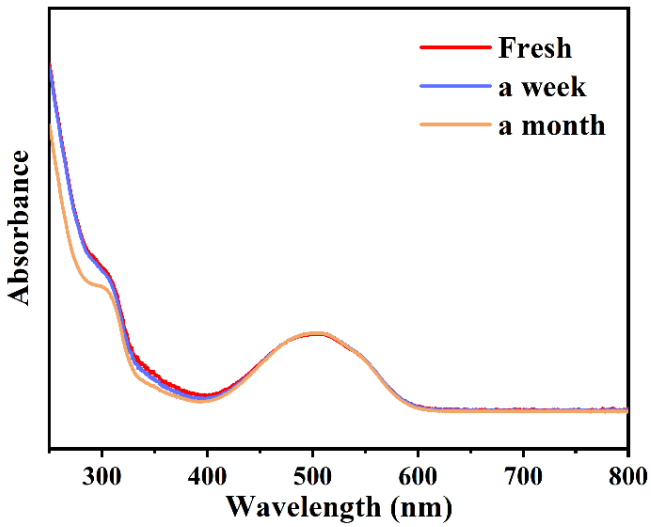

Fig. S8 UV-vis absorption of **1** (ca. 0.1 mM) dissolved in a mixed solution of acetonitrile: H_2O = 10:1 with 0.1 M Et_4NClO_4 after different times.

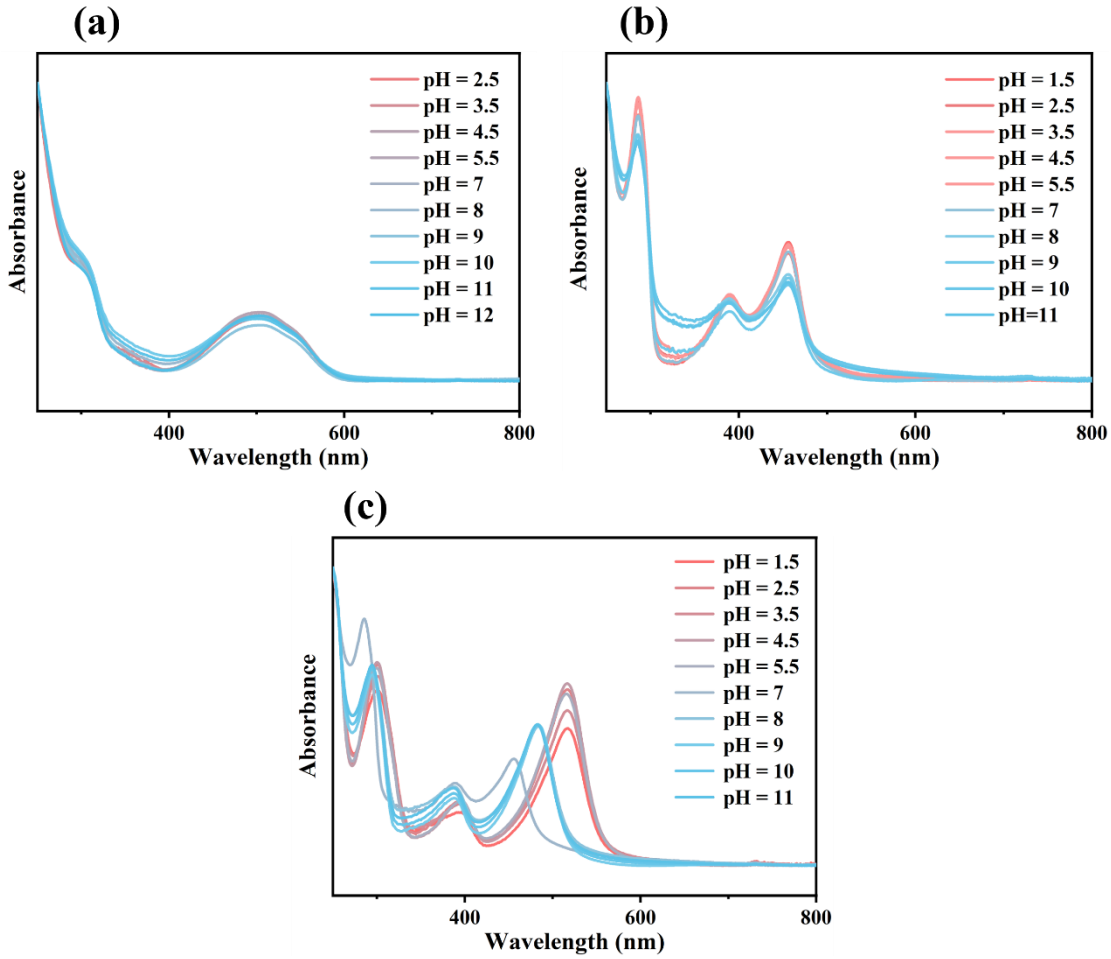

Fig. S9 UV-Vis absorption spectra of complex **1** (a), **2** (b) and **3** (c) in acetonitrile solutions (ca. 0.1 mM) with 5 M H_2O at various pH. The pH were adjusted with sulfuric acid and sodium hydroxide.

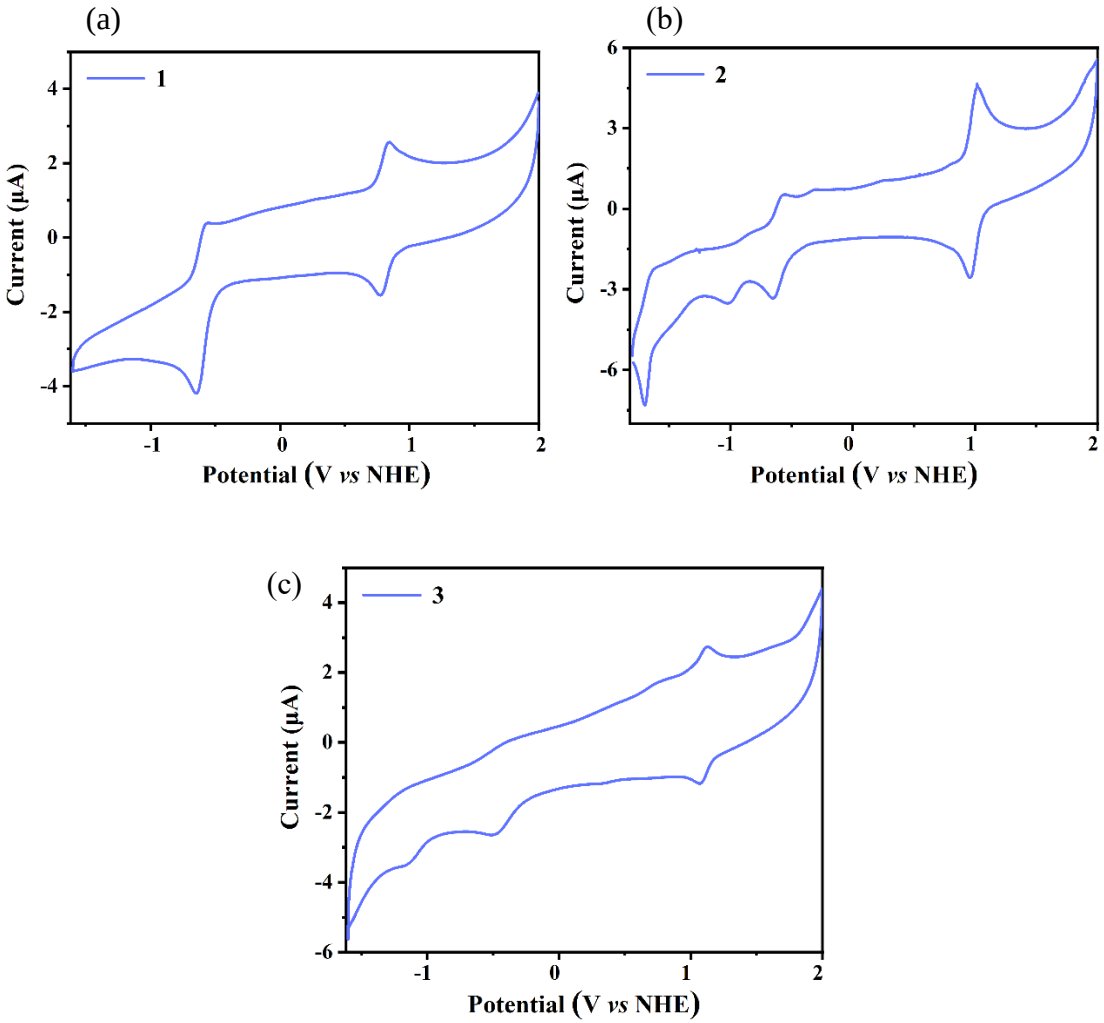

Fig. S10 CV of **1** (0.25 mM, a), **2** (0.25 mM, b) and **3** (0.25 mM, c) in an acetonitrile solution with Et_4NClO_4 (0.1 M) at a scan rate of 50 mV s^{-1}.

Table S2. Photophysical and electrochemical data of complexes **1-3**

Complexes	Abs (nm)	E_{ox} (V vs NHE)	E_{red} (V vs NHE)	ΔE (mV)
1	545, 502, 298	0.84	0.77	67.5
2	457, 390, 286	1.02	0.96	57.5
3	520, 394, 302	1.13	1.07	57.5

Ultraviolet absorption spectrum was tested in anhydrous acetonitrile, concentration of catalyst is ac. 0.1 mM; cyclic voltammetry was performed in anhydrous acetonitrile with 0.25 mM catalyst and 0.1 M Et_4NClO_4 as supporting electrolyte at room temperature. The scan rate is 50 mV/s.

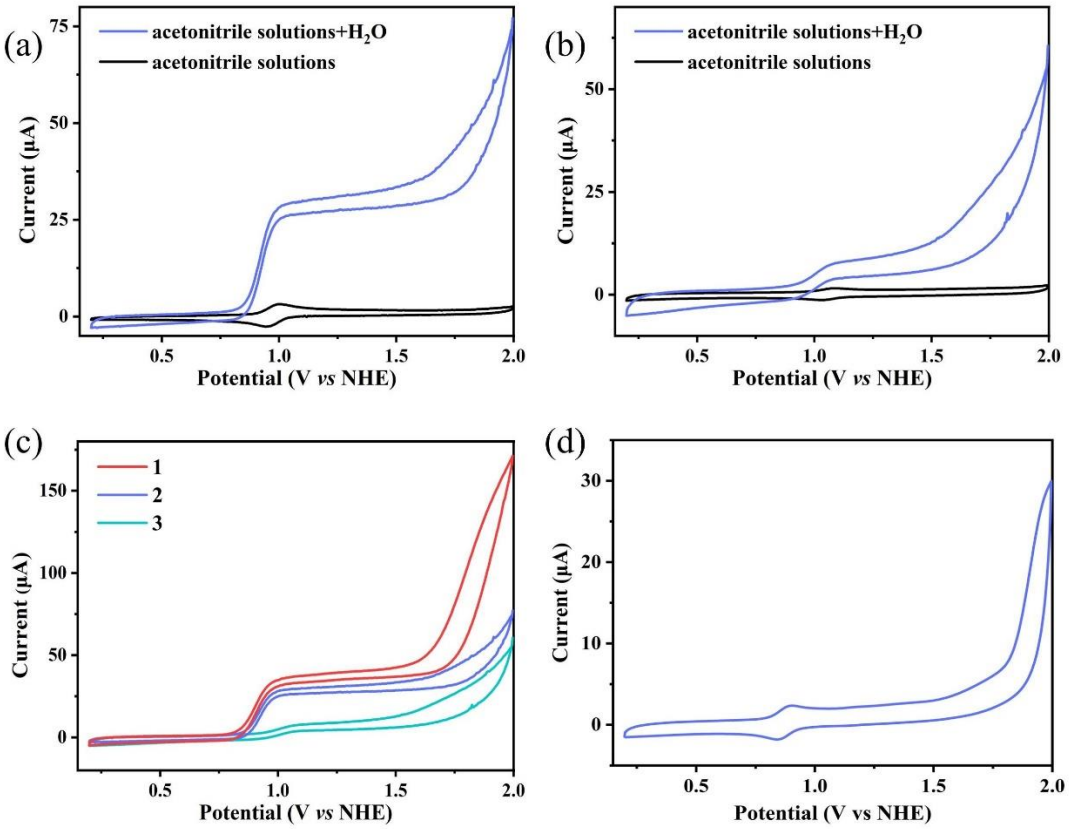

Fig. S11 CVs of **2** (0.25 mM, a) and **3** (0.25 mM, b) in acetonitrile solutions (0.1 M Et_4NClO_4) with H_2O (blue line, acetonitrile: H_2O = 10:1) and without H_2O (black line). (c) Comparison of CVs between three complexes in mixed solution of acetonitrile: H_2O = 10:1 with 0.1 M Et_4NClO_4 as the supporting electrolyte at a scan rate of 50 mV s^{-1}. (d) CV of **1** under same condition by using a glassy carbon electrode (3 mm diameter).

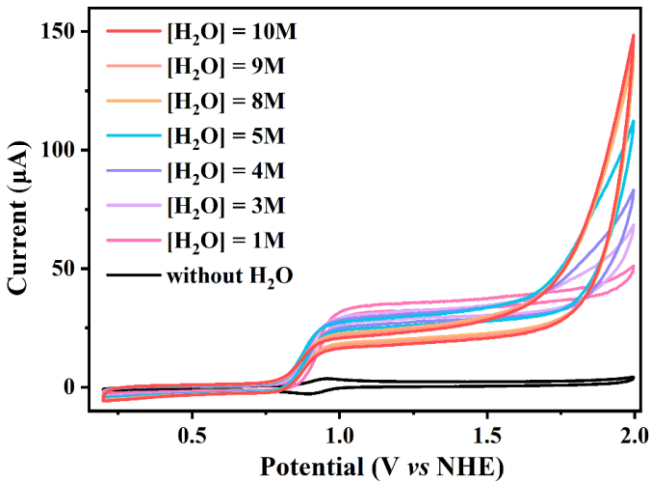

Fig. S12 Water oxidation CVs of **1** in acetonitrile solution (0.1 M Et_4NClO_4) with various concentration of deionized water.

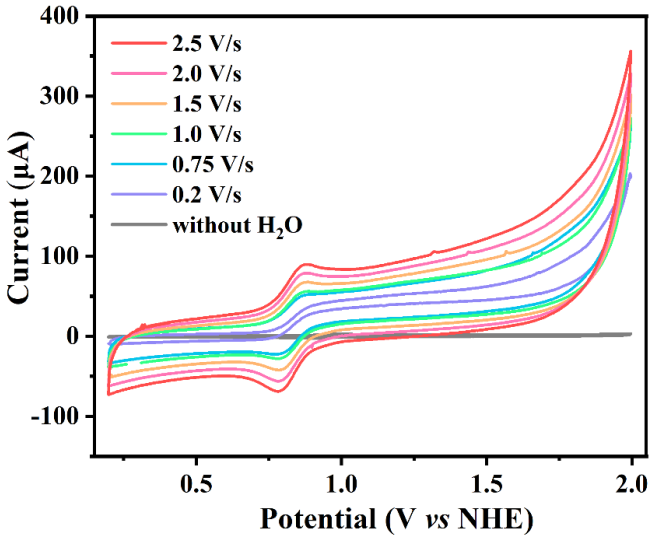

Fig. S13 CVs of **1** (0.25 mM) at various scan rates (0.2–2.5 V/s). Measurements were performed in a well-mixed solution of acetonitrile: H_2O = 10:1 with 0.1 M Et_4NClO_4 as the supporting electrolyte.

Table S3. Summary of the numerical data in the electrochemical measurements.

v (V s^{-1})	$v^{1/2}$ ($V^{1/2}$ $s^{-1/2}$)	$v^{-1/2}$ ($V^{-1/2}$ $s^{1/2}$)	i_{cat} (μA)	i_p (μA)	i_{cat} / i_p
0.2	0.45	2.24	213	28	7.61
0.75	0.87	1.15	266	52	5.13
1	1	1	272	55	4.97
1.5	1.22	0.82	302	67	4.49
2.0	1.41	0.71	328	84	3.90
2.5	1.58	0.63	357	95	3.73

Plots of i_p vs $v^{1/2}$ and i_{cat}/i_p vs $v^{-1/2}$ are shown in Fig. 4.

Calculation of Faradaic efficiency

The Faradaic efficiency of the reaction was calculated using a rotating ring (Pt)-disk (GC) electrode (RRDE) and a Pine workstation. Amperometry was used to measure the electrode collection efficiency (N) in 5.0 mM $K_3Fe(CN)_6$ and 0.1 M KCl. The disk had a potential of 0.10 V (vs Ag/AgCl) and the ring had a potential of 0.80 V (vs Ag/AgCl), and the rotation rate was 1600 rpm. The collection efficiency was determined using

$$\mathrm{N} = \frac{I_r}{I_d} \cdots\cdots\cdots\cdots\cdots\cdots\cdots\cdots (9)$$

where I_r is the ring current, I_d is the disk current.[13] *N* was determined to be 0.42 (42 %).

The current and potential were determined using the previous CV data. The disk's potential was 1.60 V (vs Ag/AgCl), ensuring the oxidation of water to generate O_2. And on the ring, the potential was -0.40 V (vs Ag/AgCl), ensuring that O_2 was able to be reduced. The formula for calculating Faraday efficiency is as follows:

$$\varepsilon = \frac{I_r}{NI_d} \cdots\cdots\cdots\cdots\cdots\cdots\cdots\cdots (10)$$

where ε is Faraday efficiency.[14] The ring current (I_r) and the disk current (I_d) was about 20 μA and 50 μA, respectively. the Faradaic efficiency was calculated to be 95 %.

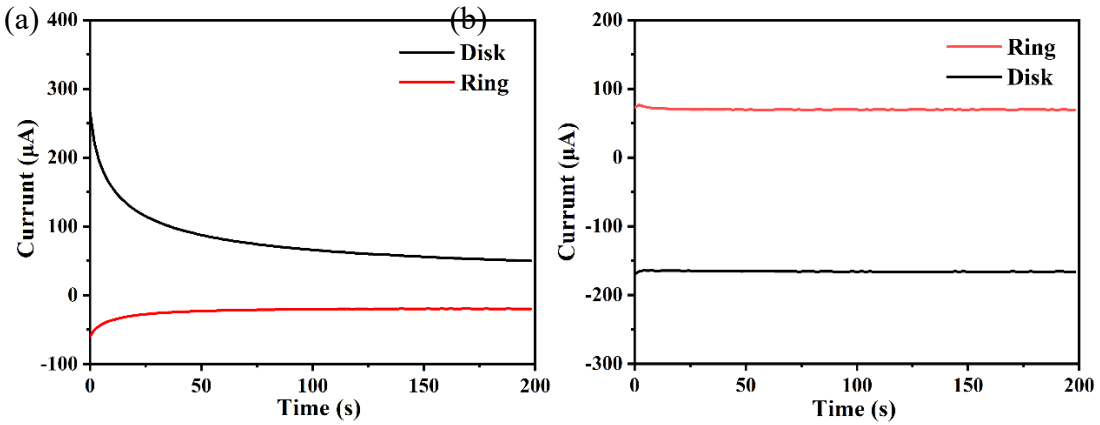

Fig. S14 Time dependence of dual electrode current. (a) Measured in 5.0 mM $K_3Fe(CN)_6$ and 0.1 M KCl; (b) Measured in a mixed solution of acetonitrile: H_2O = 10: 1 containing 0.25 mM **1** and 0.1 M Et_4NClO_4.

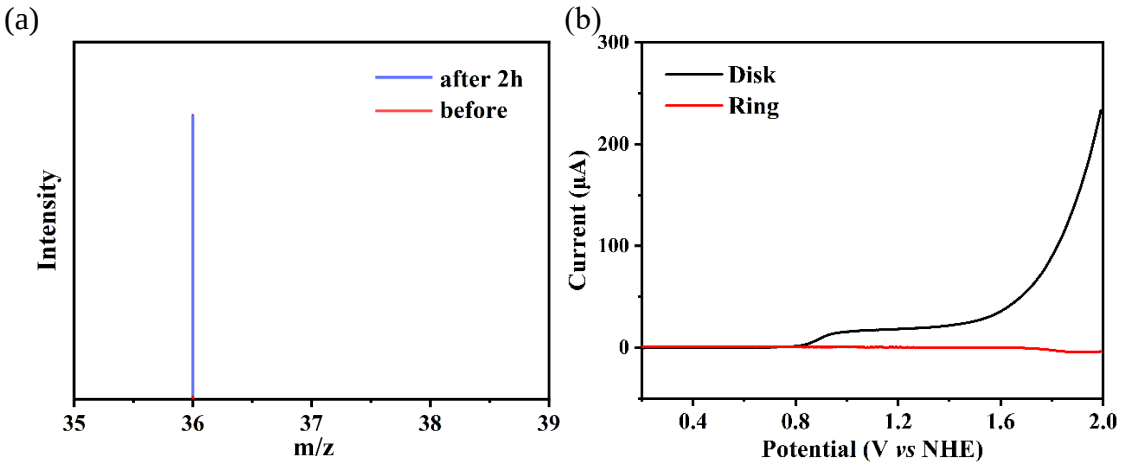

Fig. S15 (a) MS of generated gas after electrolysis (0.25 mM complex **1** in $H_2{}^{18}O$ (97 atom% ^{18}O)/acetonitrile (1:2) mixed solution with Et_4NClO_4 (0.1 M), 1.7 V vs NHE). (b) RRDE analysis of 0.25 mM **1** in H_2O/acetonitrile (1:2) mixed solution with Et_4NClO_4 (0.1 M). The potential of the ring electrode is maintained at 0.94 V vs NHE. The rotation rate is 1600 rpm, and the scan rate is 50 mV/s.

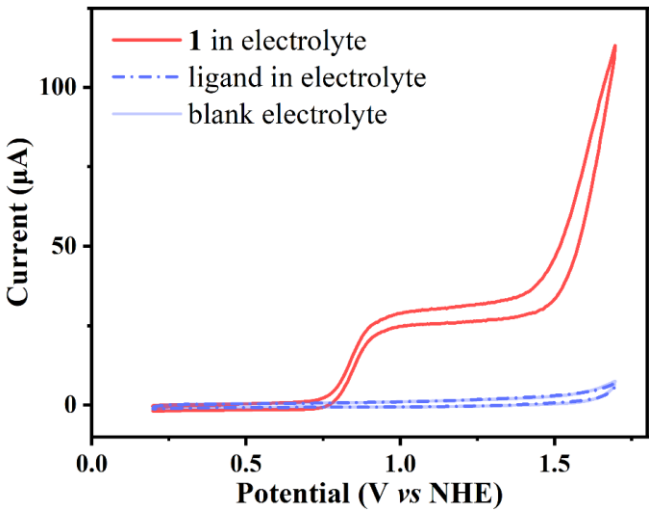

Fig. S16 CVs in electrolyte (a mixed solution of acetonitrile: H_2O = 10:1 with 0.1 M Et_4NClO_4) with **1** (0.25 mM, red line), ligand (0.25 mM, blue dashed line) and blank electrolyte (blue solid line).

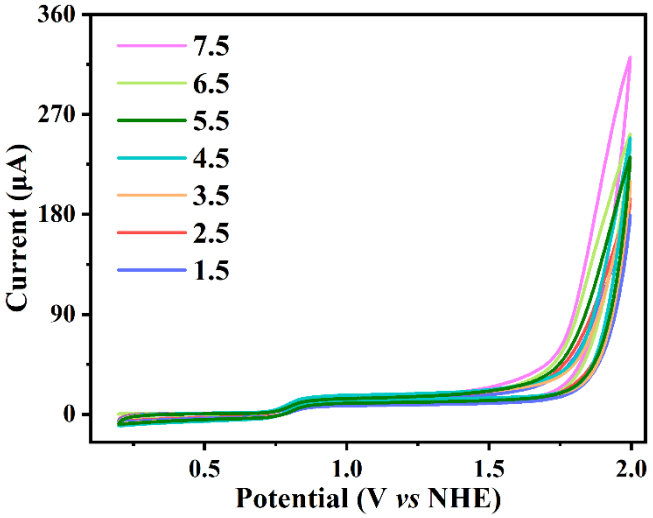

Fig. S17 CVs of 0.15 mM **1** in H_2O/acetonitrile (1:2) mixed solution with Et_4NClO_4 (0.05 M) at various pH values. The pH were adjusted with sulfuric acid.

Table S4. Comparison of performance in molecular catalysis for water oxidation

Catalyst	pH for η	electrolyte	η (mV)	FE	TOF	Reference
Complex **1**	1.5	acetonitrile/water = 10:1	490	95%	2.8 s^{-1}	This work
(Fe**L$_1$**) $(OTf)_2$	1	aqueous CF_3SO_3H solution	370		0.1 s^{-1}	[15]
[Fe**L$_2$**(Cl_2)]Cl	11	0.25 M phosphate buffer	600	91.5%	65 s^{-1}	[16]
$[Fe_2(m\text{-}O)(OH_2)_2(TPA)_2]^{4+}$	8.4	0.1M $NaHCO_3$	≈830	＞90%		[17]
[(MeOH)Fe(**L$_3$**)-μ-O-(**L$_3$**)Fe(MeOH)]$(OTf)_4$		0.1M Na_2SO_4 solution	300-400		0.12 s^{-1}	[10]
$Fe^{II}_4Fe^{III}(\mu3\text{-}O)(\mu\text{-}$**L$_4$**$)_6]^{3+}$		acetonitrile/water = 10:1	＞500	96%	1900 s^{-1}	[9]
([Ni**L$_5$**$](F_6)_2$	9	Acetate/phosphate buffer solution	800	93%		[18]
[Ru(**L$_6$**)(OH)]−	5.9	0.1M KOH solution	410	almost 100%	0.031 s^{-1}	[19]
$[Mn^{12}O^{12}(O_2CC_6H_3(OH)_2)_{16}(H_2O)_4]$	6	acetate buffer	340	77.9%		[20]
CoHβFCX-CO_2H	7	0.1 M phosphate buffer		100%	0.81 s^{-1}	[21]
(NH_4)[Cu(**L$_7$**)]$1.5H_2O$	8	2 mM $Na_2S_2O_8$ in borate buffer (0.04 M).	540	86%	0.19 s^{-1}	[22]

L$_1$ = {N,N'-dimethyl-2, 11-diaza [3.3] (2,6)pyridinophane)} $(CH_3CN)_2$

L$_2$ = 1,4,7,10-tetraazacyclododecane

L$_3$ = N,N-bis(2,2'-bipyrid-6-yl)amine

L$_4$ = dicarbonyl-(2,4-bis(trimethylsilyl)bicyclo[3.3.0]nona-1,4-dien-3-one)[1,3-dimethyl-ilidene]

L$_5$ = *bis*(2-pyridyl-methylimidazolylidene)methane, a macrocyclic NHC/pyridine hybrid ligand

L$_6$ = 4'-octyloxy-2,2':6',2''-terpyridine

L$_7$ = $(dien)(H_2O)_2]_2[\beta\text{-}VMo_7O_{26}]$

Spaces represent that the performance are not mentioned in original paper.

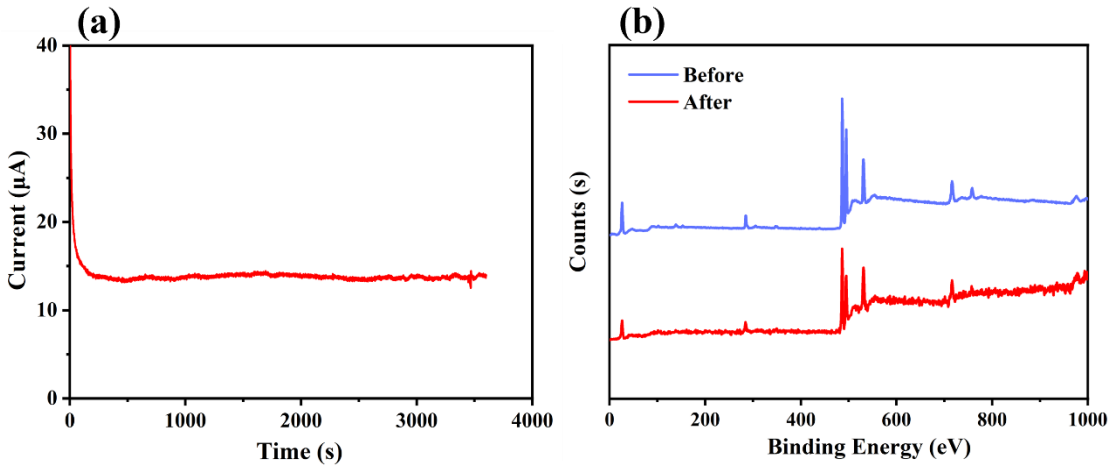

Fig. S18 (a) Time dependence of electrode current by using FTO (with an exposed area of 1 cm^2) as working electrode, (b) X-ray photoelectron spectroscopy of fresh FTO electrode (blue line) and after electrolysis under 1.7 V vs NHE for 1 h (red line). Water oxidation measurement was performed in a mixed solution of acetonitrile: H_2O = 10: 1 containing 0.25 M **1** and 0.1 M Et_4NClO_4.

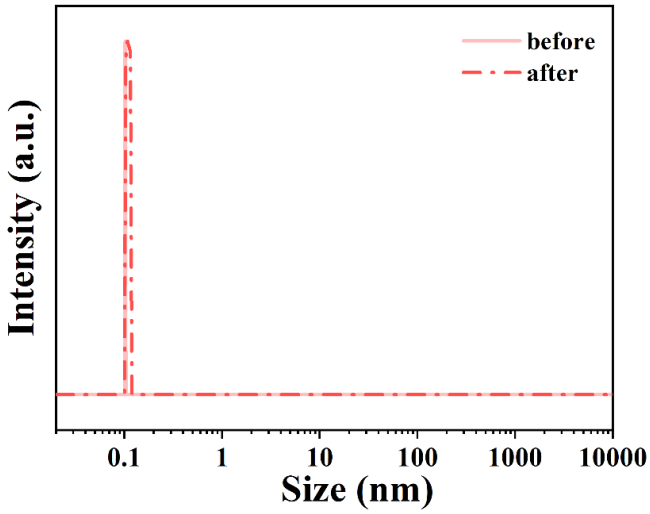

Fig. S19 Particle size distribution determined by DLS measurements before and after water oxidation under 1.7 V (vs NHE) for 1 h. Water oxidation measurement was performed in a mixed solution of acetonitrile: H_2O = 10: 1 containing 0.25 M **1** and 0.1 M Et_4NClO_4.

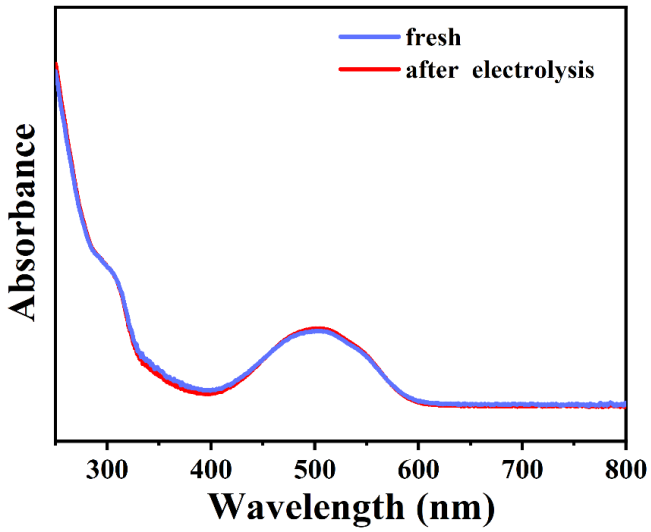

Fig. S20 UV-vis spectra of 0.25 mM **1** before (blue line) and after (red line) one hour CPE under 1.7 V (vs NHE) in a mixed solution of acetonitrile: H_2O = 10: 1 containing Et_4NClO_4 (0.1 M).

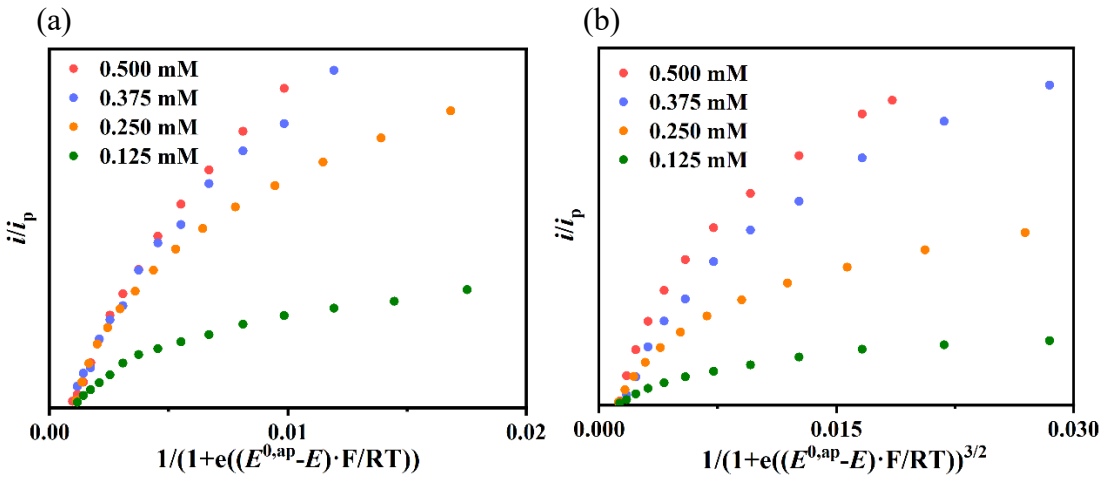

Fig. S21 (a) i/i_p vs $1/\{1+\exp[(E^0-E)F/(RT)]\}$ plots under different catalyst concentration assuming a WNA mechanism, (b) i/i_p vs $1/\{1+\exp[(E^0-E)F/(RT)]\}^{3/2}$ plots under different catalyst concentration assuming a I2M mechanism. The original CVs are shown in Fig. 3b.

Section 3: Computational method

The density functional theory (DFT) calculations were performed via the Vienna ab initio simulation package (VASP).[23] Effective potential between ionic cores and electrons was described by the projector augmented wave (PAW) method.[24] We choose the generalized gradient approximation (GGA) in the Perdew-Burke-Ernzerhof (PBE) parametrization for the exchange-correlation functional.[25] A molecule model was built, which includes 91 atoms, to study adsorption properties. The k-point sampling of the first Brillouin zone was done with a 1×1×1 Γ-centered k-points grid.[26] The energy cutoff was set to 550 eV for all cases. All the geometries were optimized using the conjugated-gradient method[27] until a Hellman-Feynman force convergence threshold of 10^{-2} eV/Å, with the energy differences are converged within 10^{-5} eV for each self-consistency iteration. To avoid the interactions between adjacent molecule, the vacuum region is set in excess of 10 Å. To describe the effective on-site Coulomb interactions of the transition-metal atoms in the molecule, the Hubbard-based DFT + U correction method[28] has been applied to all calculations and the effective value (U_{eff}) is set to be 3.5 eV. The reaction free energies, Δ*G*, are determined according to the following equation:

$$\Delta G = \Delta E_{DFT} + \Delta E_{ZPT} - T\Delta S \quad \text{..... (11)}$$

where ΔE_{DFT} is the adsorption energy of a specific step, ΔE_{ZPT} is the correction of zero point energy and Δ*S* is the change of entropy for the reaction step.

In order to explore the oxidation state of iron during water oxidation, the localized orbital bonding analysis (LOBA)[29] method was carried out to study. At first, the wavefunctions were calculated using B3LYP method,[30] and the 6-311G* basis set[31] was used for light atoms, while the SDD pseudopotential and basis set[32] were applied for Fe atoms with Gaussian 16 program package.[33] The SMD implicit solvation model[34] was used to incorporate solvation effects in water. And then the LOBA analysis was performed with Multiwfn 3.8 package[35] upon above wavefunctions.

Time-dependent density functional theory (TD-DFT) calculations were adopted at the B3LYP/6-311G*-SDD level.[30-32] The SMD implicit solvation model[34] was used to incorporate solvation effects in acetonitrile. And then UV-Vis spectrogram was obtained using the Multiwfn 3.8 package.[35]

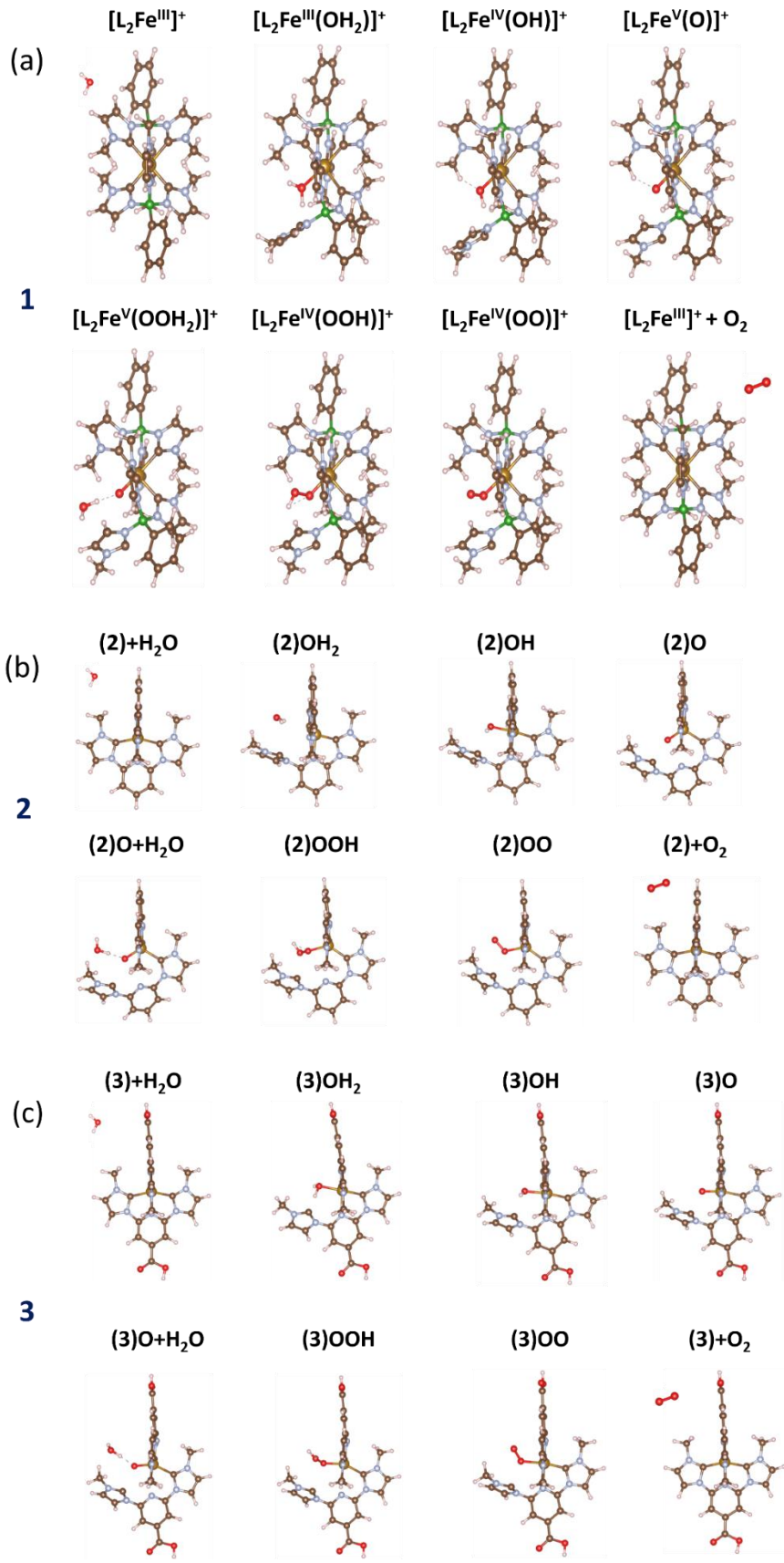

Fig. S22 The optimized configurations of (a) **1**, (b) **2** and (c) **3** in the electrochemical pathway. The values of the free energy barriers for the PDS are shown in Fig. 6a.

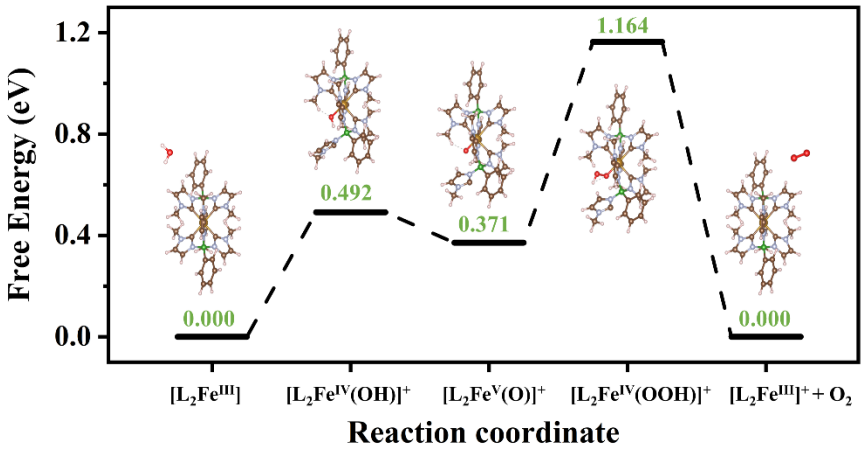

Fig. S23 Free energy diagram and the corresponding species of **1** in water oxidation (free energy versus the equilibrium potential of water).

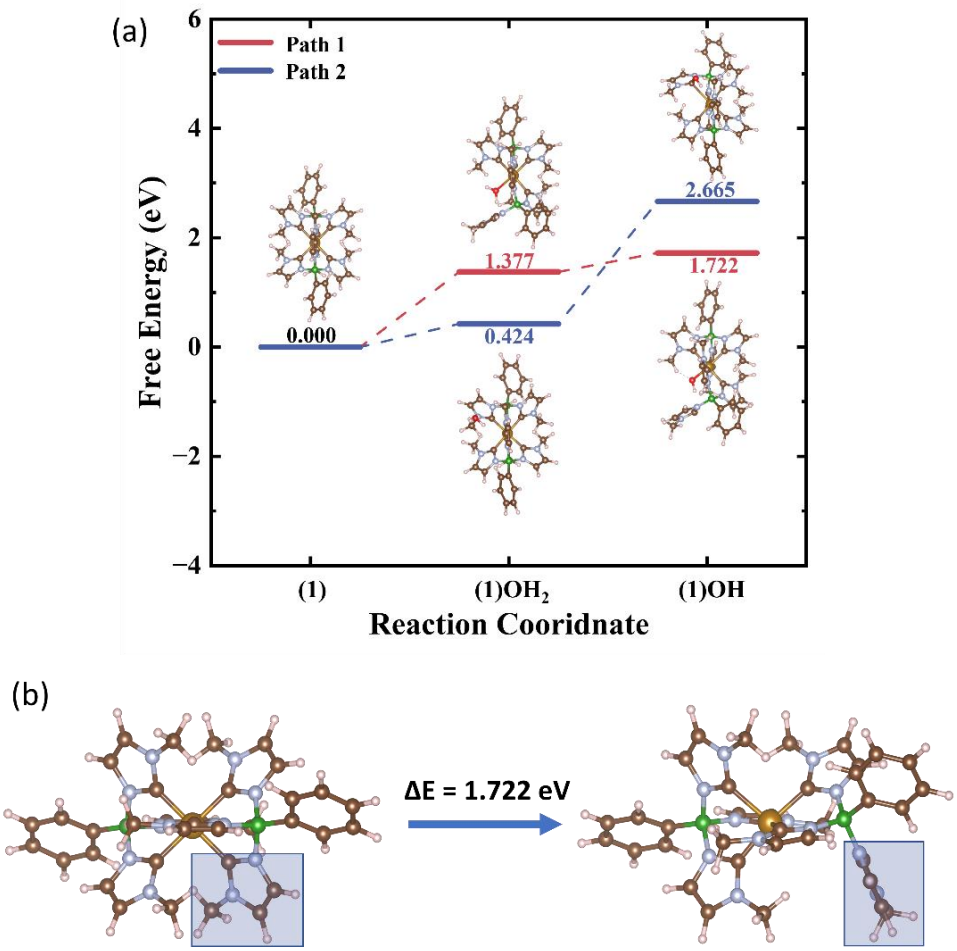

Fig. S24 (a) Free energy diagram and the corresponding species of **1** for the paths with (path 1) and without (path 2) an Fe-C bond disconnection during water oxidation. (b) Optimized structures of the original complex **1** (left) and **1** with an Fe-C bond disconnected (right).

Table S5. Net electron change of Fe and the two ligands based on Bader charge analysis.

Net electron change	**(1)OH_2**	**(1)OH**	**(1)O**	**(1)OOH**	**(1)**
Fe	-0.798	-0.912	-0.924	-0.835	-0.809
L	0.336	0.065	-0.036	-0.028	0.424
L'	0.414	0.312	0.255	0.304	0.385

L' is the one with an Fe-C bond disconnected.

Based on our free energy calculations, the ΔG from the original complex **1** to (**1**)OH is 1.722 eV. Basides, an alternative path of the first two steps without any bonds broken has also been considered. As the free energy diagram and the corresponding structures compared in Fig. S24, in the alternative path (path 2, without any bonds broken), the H_2O cannot be attached to Fe directly since the complex is coordinatively saturated. Consequently, after the first dehydrogenation step, the hydroxyl can only bind to the C atom of a ligand instead of Fe. The free energy of the aqua complex (**1**)H_2O in path 2 is lower than that in path 1 (the path discussed in the main txet) due to its better energetical stability without any bonds broken. However, the free energy of second step to form (**1**)OH in path 2 is higher than that in path 1 with the hydroxyl binding to Fe, resulting in a larger ΔG of 2.665 eV from **1** to (**1**)OH, which is much higher than that of 1.722 eV in path 1.

In addition, our calculations indicate that the structure of complex **1** with an Fe-C bond disconnected can also be optimized to a metastable configuration with the total energy 1.179 eV higher than the original one. Based on these results, the electrochemical pathway with one Fe-C bond disconnected in **1** is the most reasonable one that may happen.

Bader charge analysis was further executed to investigate the electron change on iron and the two ligands. As shown in Table S5, there is a distinct increase (decrease) for the value of net electron deficiency on Fe when the oxidation state increases (decreases) during the electrochemical process, which is consistent with the oxidation states in Fig. 6(b). In addition, the electron changes for the two ligands are generally accordant with Fe since the whole complex will contribute to the charge transfer from Fe to the attached O during the process. The major difference between the two ligands is that compared to L' (with the Fe-C bond broken), the value of net electron excess on L (with the Fe-C bond kept) decreases significantly when the first dehydrogenation step happens. This is because the broken Fe-C bond blocks the influence of the oxidation of Fe to L'.

Spectroelectrochemical method

As shown in Fig. S25, when 0.6 V (vs NHE) voltage is applied to complex **1** for 270 s, the absorption spectrum remains unchanged. When the voltage is raised to 1.0 V (vs NHE), the absorption peak of **1** decreases gradually at 502 nm and increases sharply at 715 nm and 810 nm with the passage of time. Furthermore, the absorption spectrum of complex **1** under different voltages in the range of 0.6-1.0 V (vs NHE) was performed. It is obvious that absorption peaks of complex **1** start to change when the voltage reaches 0.78 V (vs NHE). As the voltage continues to increase, the characteristic peak at 502 nm LMCT absorption gradually decreases, reflecting the oxidation of center Fe^{III} to Fe^{IV} states. In contrast, a peak at 715 nm and a pronounced shoulder around 810 nm significantly increase to form a broad absorption band in the red and near IR, which corresponds to a LMCT transition.[3] Those absorption bands suggestive of high valent iron species as reported.[36,37]

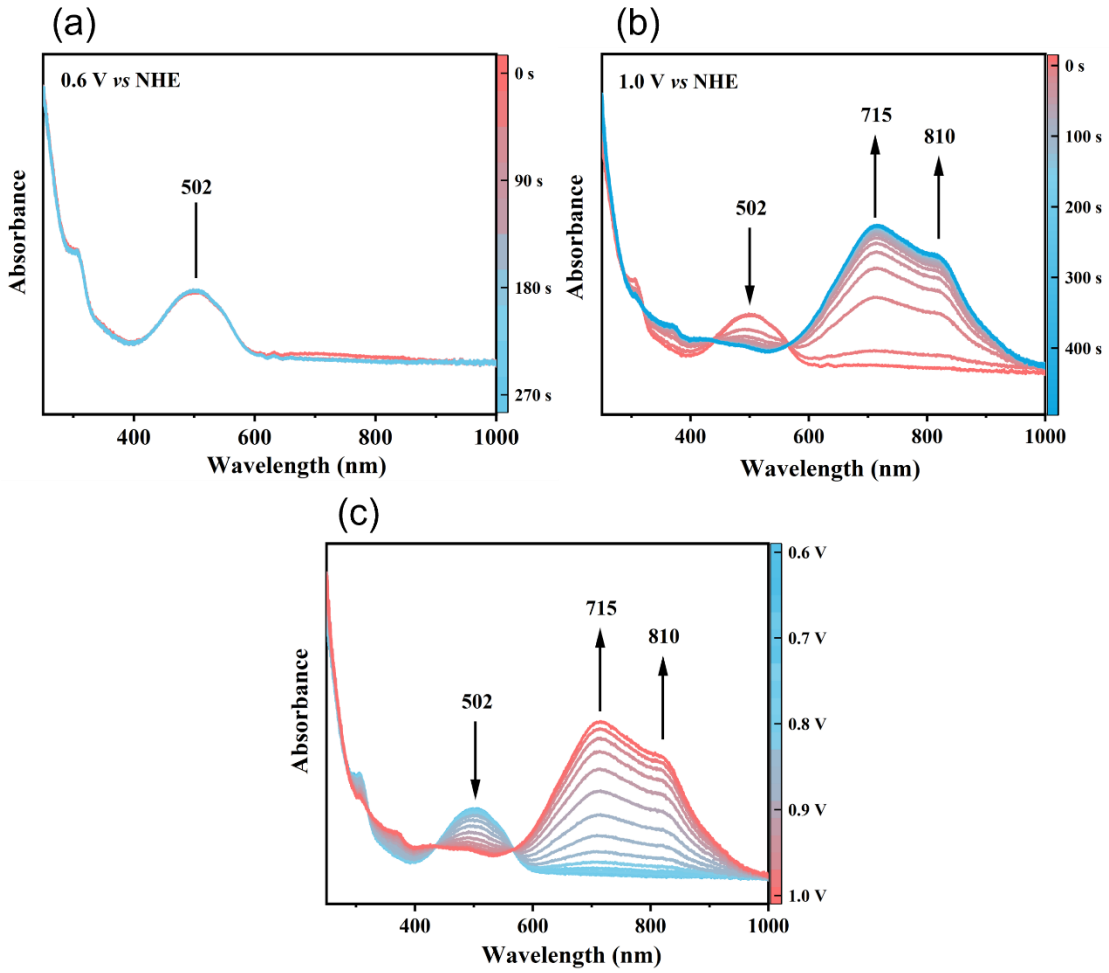

Fig. S25 Spectroelectrochemistry monitoring change in optical absorption spectrum during water oxidation by **1**, Spectral changes with time at an applied potential of (a) 0.6 V vs NHE, (b) 1.0 V vs NHE. (c) Spectral at 0.6 – 1.0 V (vs NHE) potential (the interval of potential is 0.02 V, application time is 10 s).

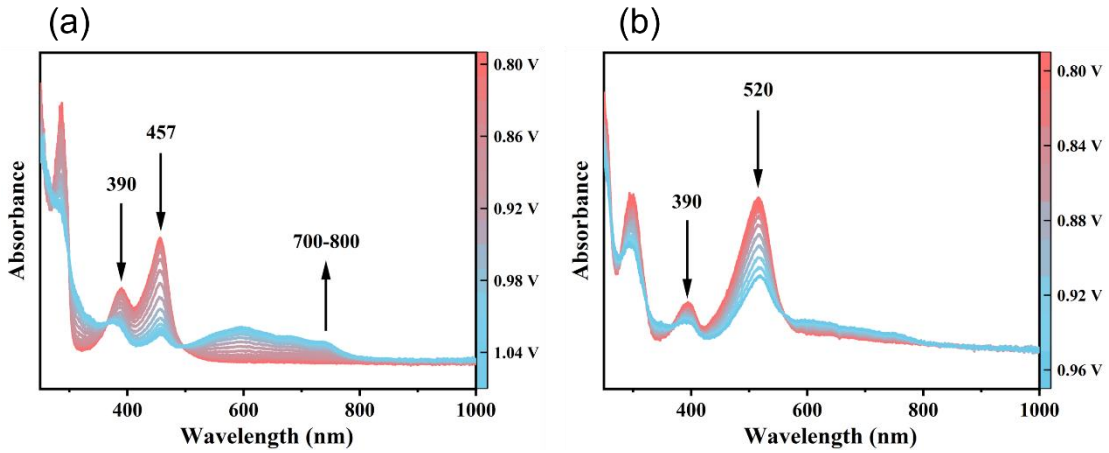

Fig. S26. Spectroelectrochemistry monitoring change in optical absorption spectrum at 0.8–1.1 V (vs NHE) potential (the interval of potential is 0.02 V, application time is 10 s) of (a) **2** and (b) **3**.

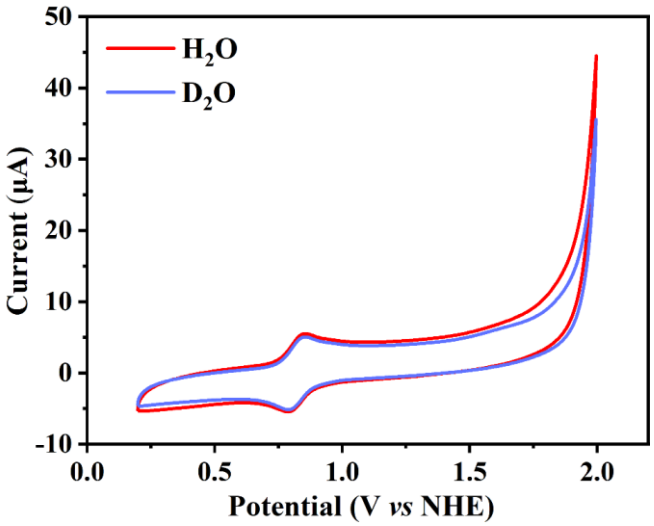

Fig. S27 CVs of **1** in H_2O and D_2O (0.25 mM, in a mixed solution of acetonitrile: H_2O (D_2O) = 10:1 with 0.1 M Et_4NClO_4).

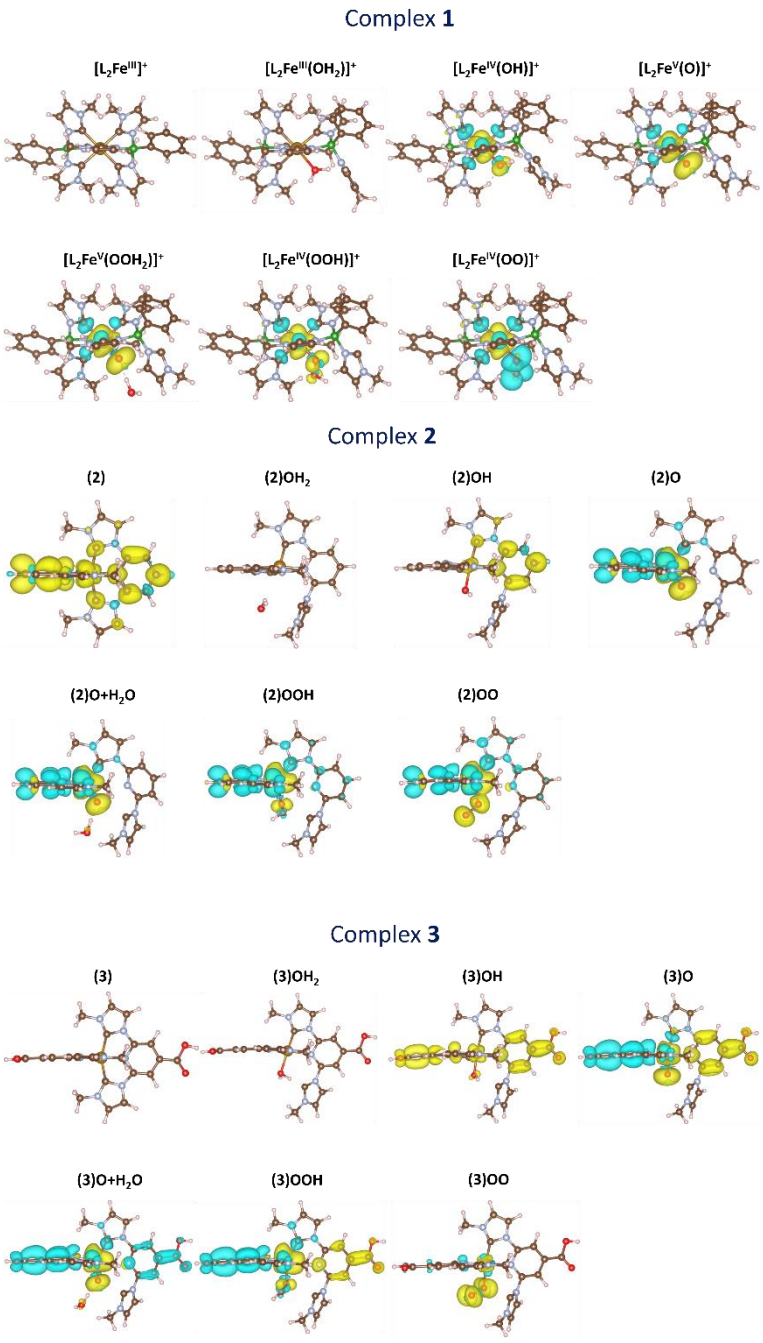

Fig. S28 The spin density distribution of the intermediates in the catalytic pathway for complexes **1**-**3**.

Reference

1 A. P. Forshaw, R. P. Bontchev and J. M. Smith, *Inorg. Chem.,* 2007, **46**, 3792-3794.

2 H. J. Park, K. H. Kim, S. Y. Choi, H. M. Kim, W. I. Lee, Y. K. Kang and Y. K. Chung, *Inorg. Chem.,* 2010, **49**, 7340-7352.

3 K. S. Kjær, N. Kaul, O. Prakash, P. Chábera, N. W. Rosemann, A. Honarfar, O. Gordivska, L. A. Fredin, K. E. Bergquist, L. Häggström, T. Ericsson, L. Lindh, A. Yartsev, S. Styring, P. Huang, J. Uhlig, J. Bendix, D. Strand, V. Sundström, P. Persson, R. Lomoth and K. Wärnmark, *Science,* 2019, **363**, 249-253.

4 T. Duchanois, T. Etienne, C. Cebrián, L. Liu, A. Monari, M. Beley, X. Assfeld, S. Haacke and P. C. Gros, *Eur. J. Inorg. Chem.,* 2015, **2015**, 2469-2477.

5 O. V. Dolomanov, L. J. Bourhis, R. J. Gildea, J. A. K. Howard and H. Puschmann, *J. Appl. Crystallogr.,* 2009, **42**, 339-341.

6 G. M. Sheldrick, *Acta Crystallogr. Sect. A Found. Crystallogr.,* 2015, **71**, 3-8.

7 G. M. Sheldrick, Acta Crystallogr. *Sect. C Struct. Chem.,* 2015, **71**, 3-8.

8 J. Xie, P. Yang, C. Tang, T. Chen, C. Zhong, L. Wang and Y. Huang, *Adv. Mater. Interfaces.,* 2021, **8**, 2101069.

9 M. Okamura, M. Kondo, R. Kuga, Y. Kurashige, T. Yanai, S. Hayami, V. K. K. Praneeth, M. Yoshida, K. Yoneda, S. Kawata and S. Masaoka, *Nature,* 2016, **530**, 465-468.

10 K. G. Kottrup, S. D'Agostini, P. H. Van Langevelde, M. A. Siegler and D. G. H. Hetterscheid, *ACS Catal.,* 2018, **8**, 1052-1061.

11 R. Matheu, S. Neudeck, F. Meyer, X. Sala and A. Llobet, *ChemSusChem,* 2016, **9**, 3361-3369.

12 Y. Liu, T. Harlang, S. E. Canton, P. Chábera, K. Suárez-Alcántara, A. Fleckhaus, D. A. Vithanage, E. Göransson, A. Corani, R. Lomoth, V. Sundström and K. Wärnmark, *Chem. Commun.*, 2013, **49**, 6412-6414.

13 S. J. Koepke, K. M. Light, P. E. Vannatta, K. M. Wiley and M. T. Kieber-Emmons, *J. Am. Chem. Soc.,* 2017, **139**, 8586-8600.

14 Y. Shao, Y. Yuan and J. Huang, *Nat. Energy.,* 2016, **1**, 1-6.

15 B. Zhang, F. Li, F. Yu, H. Cui, X. Zhou, H. Li, Y. Wang and L. Sun, *Chem. - An Asian J.,* 2014, **9**, 1515-1518.

16 Z. Q. Wang, Z. C. Wang, S. Zhan and J. S. Ye, *Appl. Catal. A Gen.,* 2015, **490**, 128-132.

17 H. T. Zhang, X. J. Su, F. Xie, R. Z. Liao and M. T. Zhang, *Angew. Chemie - Int. Ed.,* 2021, **133**, 12575-12582.

18 H. M. Shahadat, H. A. Younus, N. Ahmad, M. A. Rahaman, Z. A. K. Khattak, S. Zhuiykov and F. Verpoort, *Catal. Sci. Technol.,* 2019, **9**, 5651-5659.

19 Y. Tsubonouchi, J. Honta, T. Sato, E. A. Mohamed, Z. N. Zahran, K. Saito, T. Yui and M. Yagi, *Dalton Trans.,* 2020, **49**, 1416-1423.

20 G. Maayan, N. Gluz and G. Christou, *Nat. Catal.,* 2018, **1**, 48-54.

21 D. K. Dogutan, R. McGuire and D. G. Nocera, *J. Am. Chem. Soc.,* 2011, **133**, 9178-9180.

22 H. I. Buvailo, V. G. Makhankova, V. N. Kokozay, I. V. Omelchenko, S. V. Shishkina, A. Bieńko, M. V. Pavliuk and S. I. Shylin, *RSC Adv.,* 2021, **11**, 32119-32125.

23 G. Kresse and J. Furthmüller, *Phys. Rev. B - Condens. Matter Mater. Phys.,* 1996, **54**, 11169.

24 P. E. Blöchl, *Phys. Rev. B,* 1994, **50**, 17953.

25 J. P. Perdew, K. Burke and M. Ernzerhof, *Phys. Rev. Lett.,* 1996, **78**, 1396-1396.

26 H. J. Monkhorst and J. D. Pack, *Phys. Rev. B,* 1976, **13**, 5188.

27 M. R. Hestenes and E. Stiefel, *J. Res. Natl. Bur. Stand.,* 1952, **49**, 409.

28 V. I. Anisimov, J. Zaanen and O. K. Andersen, *Phys. Rev. B,* 1991, **44**, 943.

29 A. J. W. Thom, E. J. Sundstrom and M. Head-Gordon, *Phys. Chem. Chem. Phys.* 2009, **11**, 11297-11304.

30 A. D. Becke, *Phys. Rev. A* 1988, **38**, 3098-3100.

31 L. Lapinski, D. Prusinowska, M. J. Nowak, M. Bretner, K. Felczak, G. Maes and L. Adamowicz, *Spectrochim. Acta A* 1996, **52**, 645-659.

32 S. G. Semenov, V. M. Shakhova and M. V. Makarova, *Russ. J. Gen. Chem.* 2015, **85**, 790-795.

33 M. J. Frisch, G. W. Trucks, H. B. Schlegel, G. E. Scuseria, M. A. Robb, J. R. Cheeseman, G. Scalmani, V. Barone, B. Mennucci and G. A. Petersson, *Gaussian 16, Revision A.03*, Gaussian, Inc., Wallingford CT, 2016.

34 A. V. Marenich, C. J. Cramer and D. G. Truhlar, *J. Phys. Chem. B* 2009, **113**, 6378.

35 T. Lu and F. W. Chen, *J. Comput. Chem.* 2012, **33**, 580-592.

36 D. C. Lacy, R. Gupta, K. L. Stone, J. Greaves, J. W. Ziller, M. P. Hendrich and A. S. Borovik, *J. Am. Chem. Soc.,* 2010, **132**, 12188-12190.

37 C. Panda, J. Debgupta, D. Díaz Díaz, K. K. Singh, S. Sen Gupta and B. B. Dhar, *J. Am. Chem. Soc.,* 2014, **136**, 12273-12282.